

Hierarchical multipole topological insulators

Xiujuan Zhang^{1, #}, Zhi-Kang Lin^{2, #}, Hai-Xiao Wang^{2,3, #}, Zhan Xiong², Yuan Tian¹, Ming-Hui Lu^{1,4, †}, Yan-Feng Chen^{1,4, †}, Jian-Hua Jiang^{2, †, *},

¹*National Laboratory of Solid State Microstructures and Department of Materials Science and Engineering, Nanjing University, Nanjing, 210093, China*

²*School of Physical Science and Technology, and Collaborative Innovation Center of Suzhou Nano Science and Technology, Soochow University, 1 Shizi Street, Suzhou, 215006, China*

³*School of Physical Science and Technology, Guangxi Normal University, Guilin 541004, China*

⁴*Collaborative Innovation Center of Advanced Microstructures, Nanjing University, Nanjing, 210093, China*

[#]These authors contributed equally to this work.

[†]Correspondence and requests for materials should be addressed to joejhjiang@hotmail.com (Jian-Hua Jiang) or luminghui@nju.edu.cn (Ming-Hui Lu) or yfchen@nju.edu.cn (Yan-Feng Chen)

^{*}On leave at Department of Physics, University of Toronto, Toronto, Ontario, M5S 1A7, Canada

Topological insulators have stimulated tremendous interest in quantum materials with exotic bulk and edge states that may have applications in spintronics and quantum computation. Recently, it was predicted and observed that an insulator with a quantized quadrupole moment hosts gapped edge states and in-gap corner states, demonstrating a new paradigm of higher-order topology. Such quadrupole band topology, however, is exclusive to conventional band topology based on electric dipole polarizations. Here, we discover a new topological system, denoted as the hierarchical multipole topological insulator, which exhibits multiplexing topological phenomena with concurrent dipole and quadrupole band topologies, in sonic crystals with nonsymmorphic $p4g$ symmetry. Unlike electronic systems where topological phenomena are constrained by the band filling, acoustic systems allow access to multiple topological band gaps by changing the frequency. In our sonic crystals, the first band gap has dipolar topology which can realize acoustic quantum spin Hall effect

and topological helical edge states, while the second band gap realizes a novel anomalous quadrupole topological insulator protected by the nonsymmorphic crystalline symmetry. We observe the experimental signatures of the dipolar and quadrupolar band topologies through measurements of the corner and edge states. Our study establishes a bridge between multipole topology and subwavelength metamaterials based on multiple Bragg scattering mechanisms, and demonstrates an instance that classical systems can serve as powerful and elegant simulators for the discovery of novel topological quantum states.

The well-known Su-Schrieffer-Heeger model [1] illustrates that the quantized dipole moment of an insulator has nontrivial consequences on the surface charge [2], serving as a fundamental example of charge fractionalization [3]. The bulk dipole polarization of a crystalline insulator is quantified through the Berry phase of the Bloch bands below the band gap [4, 5]. When generalized to 2D and 3D insulators, this dipole polarization is related to the Hall conductance and magneto-electric polarizability, respectively [6-8]. Recently, quadrupole and octupole topological insulators were proposed [8, 9] as multipolar generalizations of conventional dipolar band topology. For instance, a 2D quadrupole topological insulator [8-12] supports gapped edge states with quantized dipole polarizations and in-gap, degenerate corner states at edge-terminating corners, illustrating the higher-order band topology [8-25]. A hallmark of the quadrupole topology is that, counter-intuitively, the corner charge is not an additive function of the edge polarizations but determined solely by the bulk quadrupole moment $q_{xy} = \frac{1}{2}$. As a consequence, each corner hosts only one localized mode with a fractional charge of $\frac{1}{2}$, although the polarizations of the edges terminated at a corner add up to a corner charge of 1 [8, 9].

While a quadrupole topological insulator demands vanishing dipole polarization and a finite, quantized quadrupole moment as protected by mirror symmetries [8-12, 24, 25], it is unclear whether other symmetries can also yield such nontrivial quadrupole topology. Furthermore, in electronic systems, due to the fermionic band filling, a 2D insulator can either have quadrupole or dipole topology or none of them, but cannot exhibit both band topologies.

Here, using sonic crystals of the nonsymmorphic $p4g$ symmetry, we demonstrate that glide symmetries can also lead to a nontrivial quadrupole moment, yielding a novel anomalous quadrupole topological insulator (AQTI). Conceptually, such a topological state is intriguing because the edges do not have quantized polarizations due to the absence of mirror symmetries. In fact, in our sonic crystals, the quadrupole moment vanishes when the mirror symmetries emerge (see Supplementary Information). From material perspective, our approach significantly reduces the challenge in realizing quadrupole topological insulators (QTIs). We demonstrate for the first time that quadrupole band topology can be realized in conventional acoustic metamaterials based on multiple Bragg scattering mechanisms, without fine-tuning the signs of couplings [8-12, 24, 25]. Such an advantage also gives rise to very large quadrupole topological gaps with the gap-to-mid-gap ratio reaching 37%, which leads to strong topological wave trapping at the corners and edges. Moreover, in our sonic crystals, multiplexing topological phenomena emerge because acoustic waves are not limited by band filling, as shown in Fig. 1. The concurrent dipolar and quadrupolar band topologies appear as the signature of our hierarchical multipole topological insulator.

The designed square-lattice sonic crystal (with a lattice constant $a = 2$ cm) has four arch-shaped scatterers in each unit-cell which are made of photosensitive resin (bulk modulus 2765 MPa, mass density 1.3 g/cm³, serving as “hard walls”) using the 3D printing technology (see

Materials and Methods). The geometries of the four scatterers are identical and are characterized by the arch height h , the arm length l and the arm width w , which can be tuned to engineer the acoustic bands (see Fig. 1a). Those scatterers are arranged in such a way that the sonic crystal has two glide symmetries, $G_x := (x, y) \rightarrow (\frac{a}{2} - x, \frac{a}{2} + y)$ and $G_y := (x, y) \rightarrow (\frac{a}{2} + x, \frac{a}{2} - y)$. With the inversion (i.e., parity) and the C_4 rotation symmetries, the system has a nonsymmorphic wallpaper space group of $p4g$. Previously, sonic crystals have been exploited as a remarkable platform for the simulation of topological phenomena at macroscopic scales [26-34]. Here, we use sonic crystals to discover and study a new topological state, the hierarchical multipole topological insulator.

The acoustic bands (see Fig. 1b) are obtained by solving the wave equation, $\nabla^2 P = \frac{\rho}{\kappa} \frac{\partial^2}{\partial t^2} P$ (ρ and κ are the mass density and bulk modulus, respectively) for the acoustic pressure field P , using a commercial finite-element software (see Materials and Methods). The glide symmetries have profound impact on the acoustic bands: First, the glide symmetries result in band-sticking effects [35], leading to double degeneracy on the Brillouin zone boundary lines, MX and MY. Due to such a mechanism, the first and second (the third and fourth) bands are grouped together to form a doublet. Besides, the parity of the acoustic bands is also related to the glide symmetries [12]. The parity switching between the Γ and X points (see Fig. 1b) yields a quantized dipole polarization of $\mathbf{p} = \left(\frac{1}{2}, \frac{1}{2}\right)$ for the first and second (the third and fourth) acoustic bands. Most importantly, the non-commutativity of the glide symmetries are essential for the emergence of the quadrupole band topology (see Supplementary Information for details of the above properties). Recent studies show that the wallpaper group $p4g$ leads to interesting topological phenomena within the framework of

conventional band topology [36-38]. However, quadrupole band topology has not yet been discovered in wallpaper space group crystals.

The first four acoustic bands comprise two canceling quantized dipole moments, providing a necessary condition for the quadrupole topology. The quadrupole moment of the acoustic bands, defined here through the nested Wannier bands [8, 9], is a topological quantity that governs the emergence of the quadrupole band topology, but does not have the electromagnetic meaning.

A Wannier center ν_x is the Berry phase of an energy band associated with a Wilson-loop in the Brillouin zone (e.g., with a fixed k_y while k_x runs from 0 to $\frac{2\pi}{a}$). For the first four acoustic bands, the Wannier bands are gapped and non-degenerate with two Wannier bands below the polarization gap at $\nu_x = 0$ (Fig. 1c; see Supplementary Information for calculation details). The eigenvectors of the Wilson-loops can be used to define the bulk-induced edge polarizations along the y direction, $p_y^{\nu_x^+}$ and $p_y^{\nu_x^-}$, through the nested Wannier bands above and below the polarization gap, respectively. These bulk-induced edge polarizations transform under the glide symmetries as follows,

$$p_y^{\nu_x^-} \xrightarrow{G_y} -p_y^{\nu_x^-} \bmod 1, \quad p_y^{\nu_x^-} \xrightarrow{G_x} p_y^{\nu_x^+} \bmod 1.$$

The symmetry invariance requires that

$$p_y^{\nu_x^-} = p_y^{\nu_x^+} = 0, \frac{1}{2}.$$

From the C_4 rotation symmetry, one deduce that $p_x^{\nu_y^-} = p_y^{\nu_x^-} = 0, \frac{1}{2}$ where $p_x^{\nu_y^-}$ is the bulk-induced edge polarization along the x direction. These symmetry-induced constraints result in a quantized quadrupole moment [8, 9] with $q_{xy} = 2p_y^{\nu_x^-} p_x^{\nu_y^-} = 0, \frac{1}{2}$.

The two Wannier bands below the polarization gap at $v_x = 0$ can form two distinct sectors: the “sum” sector which corresponds to the sum of the two Wannier bands, and the “difference” sector which corresponds to the difference between them. Remarkably, in our sonic crystals, the *difference* sector has gapped Wannier bands and a nontrivial quadrupole moment $q_{xy} = \frac{1}{2}$, while the *sum* sector has gapless Wannier bands and a quantized dipole moment (see Fig. 1d and see Supplementary Information for more details). These results signify an unprecedented AQTI protected by the nonsymmorphic $p4g$ symmetry, which is distinct from the QTIs protected by point group symmetries [8-12, 24, 25] and remains to be discovered. The unique nature of this AQTI (topological transition, bulk-edge-corner correspondence and other characterizations) is presented in details in Supplementary Information and in Ref. [39].

We now confirm the hierarchical multipole band topologies by experimental studies of the topological edge and corner states. Plastic cladding boards above and below the printed structure lead to a quasi-2D acoustic system, with acoustic dispersions close to the 2D limit for the low-lying bands (see Supplementary Information for supporting data). We first measure the edge states in the second acoustic band gap which are induced by the topological quadrupole moment. Here, the edge channels are formed between the sonic crystal and a hard-wall boundary made of photosensitive resin, separated by an air layer of thickness $0.25a$. The width of such an air-gap is set to exclude other non-topological mechanisms that may induce corner states (see Supplementary Information and Ref. [39]). The narrow air gap corresponds to a large cut-off frequency (34 kHz), which is much higher than the frequency of the edge states. Thus, the waveguide effect of the air-gap is excluded in the formation of the edge states studied here.

The measured edge dispersions are derived from the Fourier transformations of the frequency-dependent acoustic pressure profiles along the edge (see Materials and Methods). Despite of the fabrication precision (about ± 0.1 mm) and the finite-sample-size effect, as well as the discrepancy between the experimental quasi-2D acoustic system and the simulated 2D limit, the measured edge dispersion agrees fairly well with the simulation. These results demonstrate the emergence of gapped edge states (see Fig. 2a). The acoustic pressure profile for the edge states is measured under the acoustic excitation using a point-like source located at the middle of the edge. The simulated acoustic pressure profile under a point source excitation is presented in Fig. 2c for comparison.

Interestingly, we find that the edge states carry finite orbital angular momenta (OAM), which are manifested in two complementary ways: the phase and energy-flow distributions of the acoustic pressure fields. First, the phase distributions exhibit phase singularities and phase vortices, indicating finite OAM. The two edge states (the red and blue dots in Fig. 2a), which are time-reversal partners, have opposite phase winding numbers around the vortex cores. In addition, the distributions of the energy-flow (see Materials and Methods) of the acoustic pressure fields also indicate finite OAM for both edge states.

As shown in Fig. 2a, the quadrupole topological gap in our acoustic system ranges from 10.9 kHz to 15.7 kHz, reaching a very large gap-to-mid-gap ratio of 37%. Besides, the edge band gap ranges from 12.5 kHz to 15.3 kHz, with a large band gap ratio of 20%. These significant topological gaps lead to strong enhancement of the acoustic wave intensity for the topological edge and corner states.

We then measure the corner states in a box-shaped finite-size structure surrounded by hard-wall boundaries (see the inset of Fig. 3a). The air-gap between the sonic crystal and the hard-wall

boundary is again fixed to $0.25a$. The simulated acoustic spectrum near the edge band gap is shown in Fig. 3a. Four degenerate acoustic modes, with each of them localized at one of the four corners, emerge in the edge band gap (see Figs. 3b and 3c), which is an important signature of the quadrupole topology [8, 9]. Our simulation shows that these corner states merge into the bulk bands precisely at the topological transition point where the quadrupole topological gap closes. Besides, those corner states disappear in trivial band gaps where the quadrupole moment vanishes due to the emergence of the mirror symmetries by setting the arch-height of the scatterers to zero (see Supplementary Information for details). These results confirm that the corner states are *solely* induced by the nontrivial bulk quadrupole topology. The robustness of the corner states against disorder is studied in the Supplementary Information as well.

To confirm the coexistence of the bulk, edge and corner modes in our acoustic system, we measure the frequency-resolved responses of three different types of pump-probe configurations. We denote these pump-probe configurations as the bulk-probe, edge-probe and corner-probe, separately (see the inset of Fig. 3b). The measured transmission spectra for those pump-probe configurations are shown in Fig. 3b, where we normalize the data to set the peaks of the three curves to unity. It is seen that the peak of the corner-probe lies in the spectral gap of the edge-probe, while the peaks of the edge-probe lie in the spectral gap of the bulk-probe. In addition, the peak responses of the edge- and corner-probes are much stronger than the peak bulk response, reflecting the enhancement of the acoustic field intensity at the edges and corners due to the emergence of the edge and corner states. Bearing in mind that the second band gap has vanishing dipole polarization, those experimental observations are regarded as the key features of the nontrivial quadrupole band topology [8, 9] in our sonic crystal.

We also measure the acoustic pressure profile for one of the corner states at the peak frequency of the corner-probe. The measured acoustic pressure profile (presented in Fig. 3c) agrees well with the theoretical acoustic pressure profile obtained from the eigen-mode calculation (see Fig. 3d). Together with the pump-probe spectra, these measurements indicate that there is only one localized mode at each corner, which is another key feature of the quantized quadrupole moment [8, 9]. Note that the measured transmission spectra in Fig. 3b exhibit a small frequency blue-shift, compared with the calculated acoustic spectrum in the 2D limit in Fig. 3a, which can be associated with the small fabrication imprecision (about ± 0.1 mm) and the quasi-2D nature of the sample.

We now show that the first acoustic band gap (i.e., the dipolar topological gap) can mimic the quantum spin Hall effect (QSHE) and realize acoustic helical edge states. The double degeneracy at the Brillouin zone boundary induced by the glide symmetries provides an instrumental for the emulation of the QSHE in acoustic systems which have no internal spin degree of freedom. The emergence of the QSHE relies on the parity inversion at time-reversal invariant momenta in the Brillouin zone [6, 7]. In our sonic crystal, the band inversion can be controlled by rotating the scatterers around the center of each quarter of the unit-cell.

Noticing that rotation of the scatterers can only change the parity order at the M point, we plot the eigen-frequencies of the Bloch bands at the M point as functions of the rotation angle in Fig. 4a, where the even and odd parity bands are labeled by the blue and red curves, respectively. Parity switching takes place when the rotation angle is an integer of 90° , where a Dirac point with four-fold degeneracy emerges at the M point (see Fig. 4b). For a rotation angle between 90° and 180° , the parity of the bands below the first band gap at the M point is odd (Fig. 4a). Since these bands are of even parity at the Γ point (see Fig. 4b), the parity inversion between the Γ and M points gives rise to nontrivial band topology (i.e., the QSHE) [6, 7]. In contrast, for a rotation angle

between 0° and 90° , the parity at the M point is even, indicating no parity inversion and trivial topology. We further employ a Hamiltonian analysis of the acoustic bands near the M point using the $k \cdot p$ method, which reveals that the above two phases are similar to the QSHE and trivial phases in the Bernevig-Hughes-Zhang model [40], respectively (see Supplementary Information).

The helical edge states emerge in the first acoustic band gap at the boundary between sonic crystals with distinct topology (i.e., trivial and nontrivial), as shown in Fig. 4c. The calculated and measured (using the same method as in Fig. 2) dispersions of the acoustic edge states are consistent with each other. It is noticed that the dispersions of the edge states are not well-captured for the low-frequency part. The underlying reason is that the decreased group velocity of the edge states in the low-frequency section leads to longer propagation time and stronger propagation loss and thus yields reduced fidelity of the recorded real-space acoustic pressure profiles and the dispersions obtained from the Fourier-transformation of these profiles. The pseudospin-momentum-locking feature of the edge states is illustrated in Fig. 4d, where both the existence of phase vortices and the rotating energy-flow in the acoustic pressure profile indicate the finite OAM of the edge states. The acoustic OAM emulate the pseudospins in the acoustic helical edge states. The pseudospin-momentum-locking is manifested by the fact that the pseudospin-up and pseudospin-down edge states are connected by the time-reversal operation. Our simulation also confirms that the edge states support one-way transport when excited by acoustic sources with finite OAM (i.e., pseudospin selective excitations; see Supplementary Information). The gapless nature of the acoustic helical edge states is guaranteed by the glide symmetry on the edge which protects the double degeneracy at the $k_y = \frac{\pi}{a}$ point (see Supplementary Information for details) [21].

In summary, we have discovered a new topological system, the hierarchical multipole topological insulator, which enables multiplexing topological phenomena of competing nature (i.e.,

dipolar and quadrupolar) in a single acoustic metamaterial. Using macroscopic sonic crystals with remarkable fabrication and measurement advantages, we discover the anomalous quadrupole topological insulator protected by nonsymmorphic $p4g$ symmetry. This work also provides the first realization of quadrupole topological insulator in subwavelength metamaterials beyond the tight-binding picture. Our approach can, in principle, be generalized to other physical systems such as photonic and plasmonic systems, and thereby opens a new pathway toward topological metamaterials with multiplexing, multipolar band topologies.

References

- [1] Su, W. P., Schrieffer, J. R. & Heeger, A. J. Solitons in polyacetylene. *Phys. Rev. Lett.* **42**, 1698–1701 (1979).
- [2] Zak, J. Berry’s phase for energy bands in solids. *Phys. Rev. Lett.* **62**, 2747–2750 (1989).
- [3] Jackiw, R. & Rebbi, C. Solitons with fermion number 1/2. *Phys. Rev. D* **13**, 3398–3409 (1976).
- [4] Resta, R. Macroscopic polarization in crystalline dielectrics: the geometric phase approach. *Rev. Mod. Phys.* **66**, 899–915 (1994).
- [5] Resta, R. Quantum-mechanical position operator in extended systems. *Phys. Rev. Lett.* **80**, 1800–1803 (1998).
- [6] Hasan, M. Z. & Kane, C. L. Colloquium: Topological insulators. *Rev. Mod. Phys.* **82**, 3045–3067 (2010).

[7] Qi, X.-L. & Zhang, S.-C. Topological insulators and superconductors. *Rev. Mod. Phys.* **83**, 1057-1110 (2011).

[8] Benalcazar, W. A., Bernevig, B. A. & Hughes, T. L. Quantized electric multipole insulators. *Science* **357**, 61-66 (2017).

[9] Benalcazar, W. A., Bernevig, B. A. & Hughes, T. L. Electric multipole moments, topological multipole moment pumping, and chiral hinge states in crystalline insulators. *Phys. Rev. B* **96**, 245115 (2017).

[10] Serra-Garcia, M. *et al.* Observation of a phononic quadrupole topological insulator. *Nature* **555**, 342-345 (2018).

[11] Peterson, C. W., Benalcazar, W. A., Hughes, T. L. & Bahl, G. A quantized microwave quadrupole insulator with topological protected corner states. *Nature* **555**, 346-350 (2018).

[12] Imhof, S. *et al.* Topoelectrical circuit realization of topological corner modes. *Nat. Phys.* **14**, 925-929 (2018).

[13] Noh, J. *et al.* Topological protection of photonic mid-gap defect modes. *Nat. Photon.* **12**, 408-415 (2018).

[14] Schindler, F. *et al.* Higher-order topological insulators. *Sci. Adv.* **4**, eaat0346 (2018).

[15] Langbehn, J., Peng, Y., Trifunovic, L., von Oppen, F. & Brouwer, P. W. Reflection-symmetric second-order topological insulators and superconductors. *Phys. Rev. Lett.* **119**, 246401 (2017).

[16] Song, Z. D., Fang, Z. & Fang, C. (d-2)-dimensional edge states of rotation symmetry protected topological states. *Phys. Rev. Lett.* **119**, 246402 (2017).

[17] Ezawa, M. Higher-order topological insulators and semimetals on the breathing Kagome and pyrochlore lattices. *Phys. Rev. Lett.* **120**, 026801 (2018).

[18] Schindler, F. *et al.* Higher-order topology in bismuth. *Nat. Phys.* **14**, 918–924 (2018).

[19] Xue, H., Yang, Y., Gao, F., Chong, Y. & Zhang, B. Acoustic higher-order topological insulator on a kagome lattice. *Nat. Mater.* **18**, 108–112 (2019).

[20] Ni, X., Weiner, M., Alù, A. & Khanikaev, A. B. Observation of higher-order topological acoustic states protected by generalized chiral symmetry. *Nat. Mater.* **18**, 113–120 (2019).

[21] Zhang, X. *et al.* Second-order topology and multidimensional topological transitions in sonic crystals. *Nat. Phys.* (2019).

[22] Khalaf, E. Higher-order topological insulators and superconductors protected by inversion symmetry. *Phys. Rev. B* **97**, 205136 (2018).

[23] Fang, C. & Fu, L. Rotation anomaly and topological crystalline insulators. Preprint at <https://arxiv.org/abs/1709.01929> (2017).

[24] Franca, S., van den Brink, J. & Fulga, I. C. An anomalous higher-order topological insulator. *Phys. Rev. B* **98**, 201114 (2018).

[25] Liu, F., Deng, H.-Y. & Wakabayashi, K. Helical topological edge states in a quadrupole phase. *Phys. Rev. Lett.* **122**, 086804 (2019)

[26] Chen, Z. G. *et al.* Accidental degeneracy of double Dirac cones in a phononic crystal. *Sci. Rep.* **4**, 4613 (2014).

[27] Yang, Z. J., Gao, F., Shi, X. H., Lin, X., Gao, Z., Chong, Y. D. & Zhang, B. L. Topological acoustics. *Phys. Rev. Lett.* **114**, 114301 (2015).

[28] Ni, X. *et al.* Topologically protected one-way edge mode in networks of acoustic resonators with circulating air flow. *New J. Phys.* **17**, 053016 (2015).

[29] Xiao, M. *et al.* Geometric phase and band inversion in periodic acoustic systems. *Nat. Phys.* **11**, 240-244 (2015).

[30] He, C., Ni, X. Ge, H., Sun, X. C., Chen, Y.-B., Lu, M.-H., Liu, X.-P. & Chen, Y.-F. Acoustic topological insulator and robust one-way sound transport. *Nat. Phys.* **12**, 1124-1129 (2016).

[31] Lu, J., Qiu, C., Ye, L., Fan, X., Ke, M., Zhang, F., Liu, Z. Observation of topological valley transport of sound in sonic crystals. *Nat. Phys.* **13**, 369-374 (2017).

[32] Xiao, M., Chen, W. J., He, W. Y. & Chan, C. T. Synthetic gauge flux and Weyl points in acoustic systems. *Nat. Phys.* **11**, 920-924 (2015).

[33] Li, F. *et al.* Weyl points and Fermi arcs in a chiral phononic crystal. *Nat. Phys.* **14**, 30-34 (2017).

[34] He, H. *et al.* Topological negative refraction of surface acoustic waves in a Weyl phononic crystal. *Nature* **560**, 61-64 (2018).

[35] Parameswaran, S. A., Turner, A. M., Arovas, D. P. & Vishwanath, A. Topological order and absence of band insulators at integer filling in non-symmorphic crystals. *Nat. Phys.* **9**, 299-303 (2013).

[36] Wang, H.-X., Chen, Y., Hang, Z. H., Kee, H.-Y. & Jiang, J.-H. Type-II Dirac photons. *npj Quantum Materials* **2**, 54 (2017).

[37] Lin, J. Y., Hu, N. C., Chen, Y. J., Lee, C. H. & Zhang, X. Line nodes, Dirac points and Lifshitz transition in 2D nonsymmorphic photonic crystals. *Phys. Rev. B* **96**, 075438 (2017).

[38] Wieder, B. J. *et al.* Wallpaper fermions and the nonsymmorphic Dirac insulator. *Science* **361**, 246-251 (2018).

[39] Lin, Z.-K., Wang, H.-X., Lu, M.-H. & Jiang, J.-H. Nonsymmorphic topological quadrupole insulator in sonic crystals. Preprint at <https://arxiv.org/abs/1903.05997> (2019).

[40] Bernevig, B. A., Hughes, T. L., & Zhang, S.-C. Quantum spin Hall effect and topological phase transition in HgTe quantum wells. *Science* **314**, 1757-1761 (2006).

Acknowledgements

J.H.J thanks Arun Paramekanti and Hae-Young Kee for helpful discussions. He also thanks Sajeev John and the University of Toronto for hospitality where this work is finalized. **Fundings:** X.J.Z, Y.T, M.H.L and Y.F.C are supported by the National Key R&D Program of China (2017YFA0303702, 2018YFA0306200) and the National Natural Science Foundation of China (Grant No. 11625418 and No. 51732006). Z.K.L, H.X.W and J.H.J are supported by the Jiangsu

Province Distinguished Professor Funding and the National Natural Science Foundation of China (Grant No. 11675116). **Author contributions:** J.H.J conceived the idea and initiated the project. J.H.J, Y.F.C and M.H.L guided the research. J.H.J, Z.K.L and H.X.W established the theory. Z.K.L, X.J.Z, X.Z and H.X.W performed the numerical calculations and simulations. X.J.Z and Y.T achieved the experimental set-up and measurements. X.J.Z, J.H.J and M.H.L performed data-analysis. All the authors contributed to the discussions of the results and the manuscript preparation. J.H.J, X.J.Z, Z.K.L and M.H.L wrote the manuscript. **Competing interests:** The authors declare no competing interests. **Data and materials availability:** All data are available in the manuscript and the Supplementary materials.

Materials and Methods: Our sonic crystals consist of arch-shaped scatterers made of photosensitive resin (modulus 2765 MPa, density 1.3 g/cm³). A stereo lithography apparatus (with a fabrication tolerance of roughly 0.1 mm) is utilized to fabricate the samples, which include two ribbon-like samples for the edge-state measurements, and a box-shaped sample for the corner-state measurements, with $h = 0.212a$, $l = 0.424a$ and $w = 0.1a$, where $a = 2$ cm is the lattice constant. The vertical height of the sample is 1 cm. Two acoustic hard boards are used for cladding from the top and the bottom of the sample to form quasi-2D acoustic systems for the frequency range of interest (i.e., less than 20 kHz). The measured edge-state dispersions are obtained by the following procedure. We first scan the acoustic pressure field distribution along the edge for mono-frequency excitations. An acoustic transducer is placed under the sample to generate acoustic waves, which are further guided into the sample through an open channel (with a diameter of ~4 mm) at the bottom of the waveguide. The channel is located at the center of the edge (marked by the red star in Fig. 3B). An acoustic detector (B&K-4939 1/4-inch microphone), whose position can

be controlled by an automatic stage, is used to probe the spatial dependence of the acoustic pressure from a circular open window (with a diameter slightly larger than the detector) on the top of the cladding layer. The data are collected and analyzed by a DAQ card (NI PCI-6251). The measured acoustic pressure profiles at different frequencies are then Fourier-transformed to obtain the edge-state dispersions. The Fourier transformation is implemented by using the Matlab built-in function *fft*. The transmission measurements are performed using a similar set-up, but with fixed positions of the source and the detector when the frequency is varied.

In the experimental measurements, the upper board of the waveguide (which is attached to an automatic stage) is required to be able to move freely, but without affecting the stabled samples, in order to record the acoustic pressure filed data. To accomplish this goal, we leave a tiny air gap (about 1 mm) between the upper board and the samples below it. This treatment might affect our measurements and could be another reason (additional to the fabrication imperfection) that the measurements are slightly deviated from the simulations on frequencies. Additionally, the condition for the environment atmosphere that varies upon weather change might also affect the sound speed and the air mass density and is the third reason to the frequency shift between the experiments and the simulations.

Numerical simulations are performed using a commercial finite-element simulation software (COMSOL MULTIPHYSICS) via the acoustic module. The resin objects are treated as hard boundaries. In the eigen-value calculations, the Floquet periodic boundaries are implemented. The projected band structures of the ribbon-like supercells and the band spectrum of the box-shaped supercell are calculated by setting the truncation boundaries as hard boundaries. For the simulated acoustic-pressure distributions of the edge and corner states, the frequency-domain study is performed. A point source, located at the center of the edge (near the corner), is utilized to excite

the edge (corner) states. The energy flow is calculated through the time-averaged Poynting vector of the acoustic fields, following $\mathbf{S} = -(4\pi\rho f)^{-1}|p|^2\nabla\phi$, where ρ is the density of air, f is the eigen-frequency, and $|p|$ and ϕ are the amplitude and the phase of the acoustic pressure profile, respectively.

The transmission spectra presented in Fig. 3b are normalized by the maximum of each measurement (i.e., the bulk-probe, edge-probe and corner-probe, respectively), so that they can be plotted at the same quantitative scale. The original transmission spectra are presented separately in the Supplementary Information for the bulk-, edge- and corner-probes, separately. We find that the corner-probe yields a much stronger signal, more than 80 times stronger than the bulk-probe, indicating very strong enhancement of the acoustic wave intensity due to the strongly localized, subwavelength corner mode.

Figures

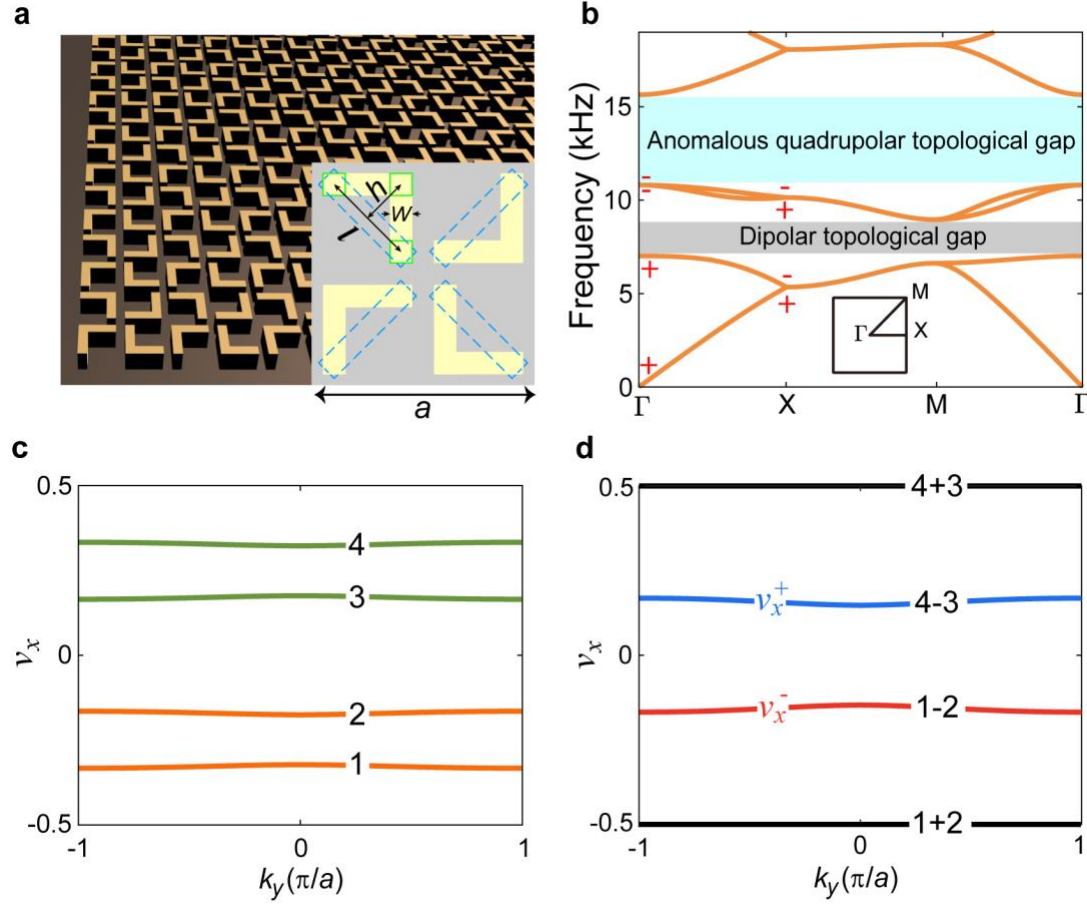


Figure 1 | Hierarchical multipole topological insulator realized in a sonic crystal. a, A bird's-eye view of a square-lattice air-borne sonic crystal comprising arch-shaped scatterers made of photosensitive resin. Inset illustrates a unit-cell. **b,** Acoustic bands and hierarchical multipole topology: dipolar and (anomalous) quadrupolar topological band gaps. Inset: Brillouin zone. Symbols $+$ / $-$ represent even/odd parity, respectively, at the Γ and X points. **c,** Gapped and nondegenerate Wannier bands for the acoustic bands below the quadrupole topological gap. **d,** Wannier bands in different sectors. Geometry parameters are $h = 0.21a$, $l = 0.42a$, $w = 0.1a$ and $a = 2$ cm.

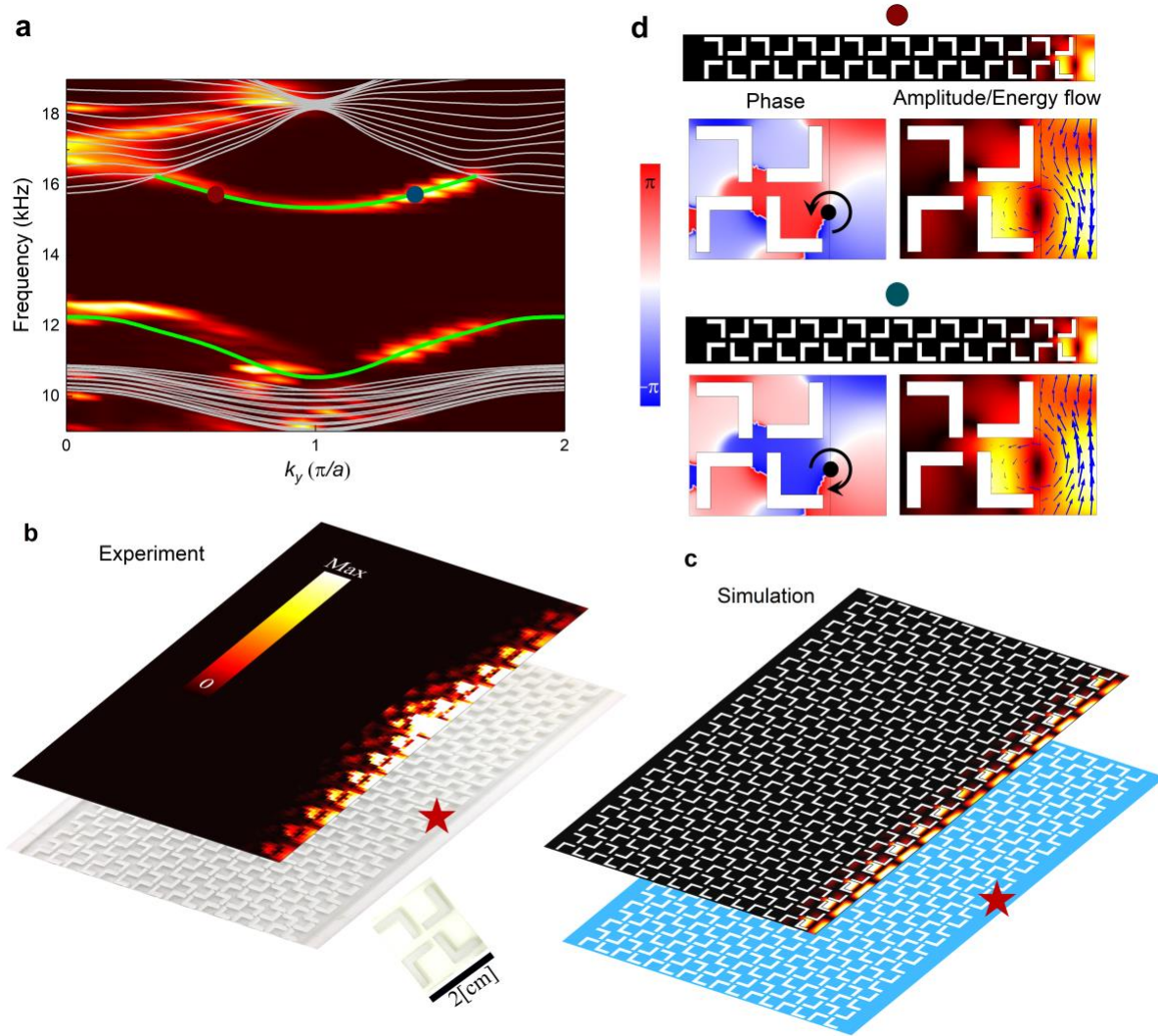


Figure 2 | Gapped topological edge states in the quadrupolar band gap. **a**, Measured (hot color) and calculated (green curves) dispersions of the acoustic edge states. Gray curves represent calculated acoustic bulk bands. **b** and **c**, top: measured and simulated acoustic pressure profiles of the edge states launched by a point-like source (indicated by the red star), respectively; underneath: photo of the fabricated sample and illustration of the structure, respectively. Inset in **b**: photo of a unit-cell. **d**, Acoustic pressure profiles for the two edge states marked by the red and blue dots in **a**, with phase, amplitude and Poynting vector (blue arrows) shown near the edge. Phase vortex

centers and phase winding directions are marked by black dots and arrows, respectively. Unit-cell geometry parameters are the same as in Fig. 1.

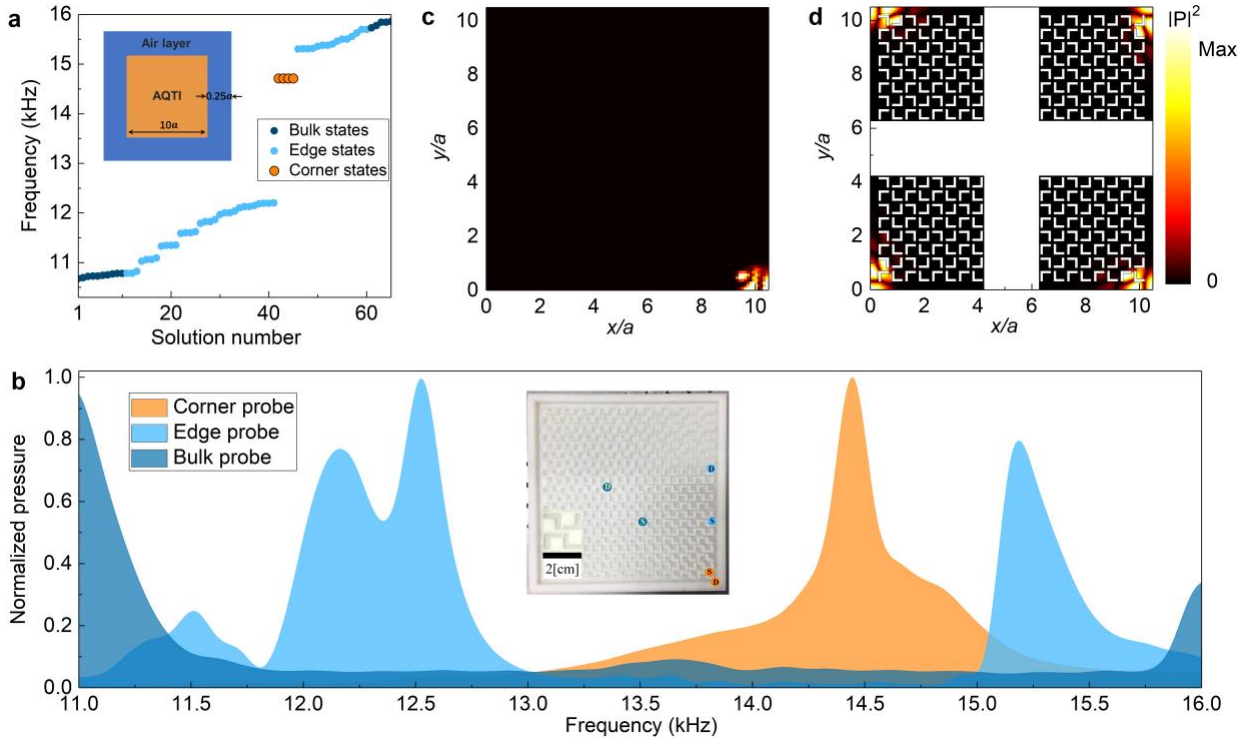


Figure 3 | Bulk, edge and corner modes around the anomalous quadrupolar topological gap.

a, Calculated acoustic spectrum for a box-shaped structure (illustrated in the inset) which has an area of $10 \times 10a^2$ and is enclosed by hard-wall boundaries with an air-gap of $0.25a$. **b**, Frequency-resolved transmission spectra for three pump-probe configurations: bulk-probe, edge-probe and corner-probe. Inset: photo of the sample with a zoom-in structure of the unit-cell. Source “S” and detector “D” for each pump-probe configuration are marked in the inset with the same color as that of the corresponding transmission curve. **c** and **d**, measured and simulated acoustic pressure profiles of corner modes, respectively. Four degenerate corner states (related by C_4

rotation) are shown in **d**, while only one of them is measured in **c**. Unit-cell geometry parameters are the same as in Fig. 1.

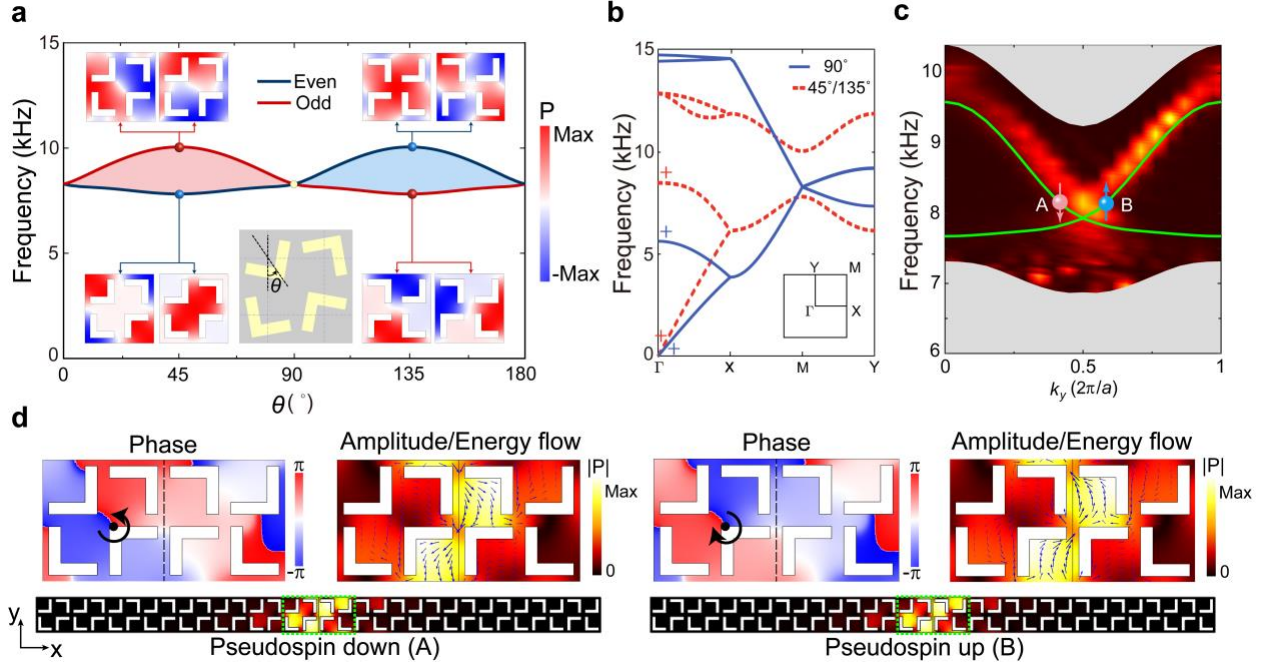


Figure 4 | Acoustic quantum spin Hall effect and helical edge states in the dipolar band gap.

a, Frequency evolution of first four acoustic bands at the M point (including two doublets of opposite parities) by tuning angle θ (defined in the inset) for $h = 0.18a$, $l = 0.35a$ and $w = 0.1a$. Acoustic pressure profiles of the doublets at the four marked points are shown. **b**, Acoustic bands for $\theta = 90^\circ$, 45° and 135° . Symbols $+$ / $-$ represent even/odd parity at Γ point, respectively. **c**, Measured (hot color) and calculated (green curves) dispersions of helical edge states at the boundary between two sonic crystals with different θ (45° and 135°) for $h = 0.21a$, $l = 0.42a$ and $w = 0.1a$. The gray regions denote bulk bands. **d**, Acoustic pressure profiles for two edge states marked by the red and blue dots in **c**, with amplitude (hot color), Poynting vectors (blue arrows) and phase shown near the boundary (the green-box regions).